Regular Article

Constructing efficient mixed-ion perovskite solar cells based on TiO$_2$ nanorod array

Longkai Yang [a], Xin Wang [a], Xianmin Mai [b,*], Tan Wang [c], Chao Wang [d,e], Xin Li [a,*], Vignesh Murugadoss [d,f], Qian Shao [g], Subramania Angaiah [f,*], Zhanhu Guo [d,*]

[a] Pen-Tung Sah Institute of Micro-Nano Science and Technology, Xiamen University, Xiamen 361005, China
[b] School of Urban Planning and Architecture, Southwest Minzu University, Chengdu 610041, China
[c] College of Chemistry and Chemical Engineering, Xiamen University, Xiamen 361005, China
[d] Integrated Composites Laboratory (ICL), Department of Chemical & Biomolecular Engineering, University of Tennessee, Knoxville, TN 37996, United States
[e] College of Materials Science and Engineering, North University of China, Taiyuan 030051, China
[f] Electrochemical Energy Research Lab, Centre for Nanoscience and Technology, Pondicherry University, Puducherry 605 014, India
[g] College of Chemical and Environmental Engineering, Shandong University of Science and Technology, Qingdao 266590, China

GRAPHICAL ABSTRACT
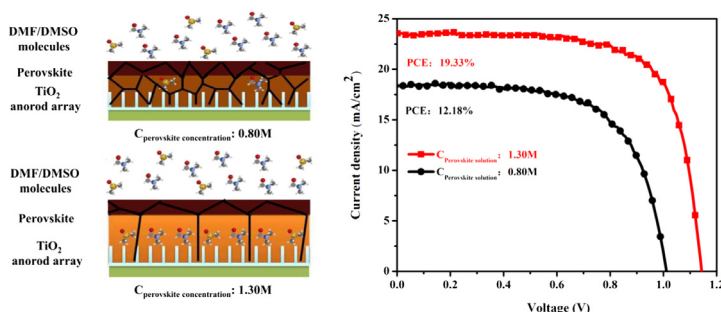
ARTICLE INFO

ABSTRACT

Oriented TiO$_2$ nanorod array (TiO$_2$ NA) is very attractive in the fields of halide perovskite solar cells (PSCs) due to its fewer grain boundaries and high crystallinity for effective charge collection. The optimization of TiO$_2$ nanostructures has been proved to be an effective approach for efficient PSCs. On the other hand, tuning the crystallization of perovskite films on top of the TiO$_2$ NA is very important for efficient TiO$_2$-NA based PSCs. Herein, scanning electron microscopy (SEM) and X-ray powder diffraction (XRD) were used to study the crystallization of different mixed-ion Cs$_{0.1}$(FA$_{0.83}$MA$_{0.17}$)$_{0.9}$Pb(I$_{0.83}$Br$_{0.17}$)$_3$ perovskite (in which MA = CH$_3$NH$_3^+$, and FA = CH(NH$_2$)$_2^+$) films, from different perovskite precursor concentrations, on the TiO$_2$ nanorod arrays. A mechanism was proposed to reveal the inherent connection between the precursor concentration and the crystallite growth of the perovskite film prepared with anti-solvent quenching process. Meanwhile, both faster charge separation at perovskite/TiO$_2$ NA interface and longer charge transport were observed on thicker perovskite film with larger grains, revealed by the time-resolved method. However, atomic force microscopy (AFM) results indicated that too thick perovskite film impaired the charge collection owing to the increased recombination. By balancing the charge collection and film thickness, highly efficient PSCs were prepared with a champion power

* Corresponding authors.
E-mail addresses: maixianmin@foxmail.com (X. Mai), lixin01@xmu.edu.cn (X. Li), a.subramania@gmail.com (S. Angaiah), zguo10@utk.edu (Z. Guo).

conversion efficiency (PCE) of 19.33% with little hysteresis. The study highlights a great potential of incorporating oriented one-dimensional electron extraction materials in high-performance PSCs and other applications.

1. Introduction

Since the first report of hybrid lead halide perovskite materials in the photoelectrochemical solar cells in 2009 [1], the rapidly increased power conversion efficiency (PCE) has been made in the field during the past nine years [2–5]. Many device architectures, preparation methods, and compositions of hybrid lead halide perovskite materials have been intensively studied to obtain efficient solar cells. For perovskite solar cells, such rapid development is inseparable from the foundation laid in the fields of dye sensitized solar cells (DSSCs) and organic solar cells (OSCs), which can learn from each other and develop together [6–8]. TiO_2 is a good example. TiO_2 films as *n*-type charge selective contact, including compact films [9], mesoporous structured films [5], and ordered structure films [10], have yielded the highest efficiencies so far. Although the nanoparticle-structured TiO_2 film can collect the photon-induced electrons efficiently for state-of-the-art perovskite solar cells, the randomly distributed nanoparticles may cause a scattering of free electrons and reduced electron mobility. Thus, tremendous efforts have been made to prepare ordered structured TiO_2 films, such as nanotubes [11,12], nanorods [13–15], and nanoforests [16], to develop a potential electron transport layer with a higher electron mobility for efficient perovskite solar cells.

Among these oriented structures, TiO_2 arrays (NAs) exhibited the greatest potential for efficient perovskite solar cells (PSCs) to date owing to their low grain boundaries, higher electron transport mobility, and open structure for the penetration of perovskite crystals [17]. Moreover, TiO_2-NA based perovskite solar cells (TiO_2-NAPSCs) show a huge advantage on the photovoltaic performance over other one-dimensional metal-oxide based PSCs [18–20]. A very recently published work by Liu et al. has presented a small-scale PSC, based on $CH_3NH_3PbI_3$ (MAPbI$_3$) absorber and TiO_2 NAs, with a PCE of 19.02%, which is comparable to that of the traditional mesoporous-TiO_2 based perovskite solar cells [21]. However, most of the reported efficient PSCs using TiO_2 NAs are based on MAPbI$_3$ perovskite [17,21], which has concerns with respect to thermal stability [22], degradation upon contact with moisture [4], sunlight stability [23], and the structural phase transition at 55 °C [24]. Researchers found that perovskite absorbers based on mixed cations and halides (mixed perovskite) are more suitable for photovoltaic applications thanking to their good photovoltaic performance, thermal and structural stabilities [25–27]. Therefore, the fabrication of PSCs based on TiO_2 NAs and mixed perovskite can provide a new approach for efficient and stable PSCs. To date, there are few reports on the fabrication of efficient PSCs with the combination of TiO_2 NAs as electron transfer layer (ETL) and mixed-ion perovskite absorbers [12–16].

The preparation of high-quality mixed-ion perovskite film on TiO_2 NAs by anti-solvent quenching method is very important to obtain good photovoltaic performance [17]. The precursor concentration and annealing temperature have been regarded as the key fabrication parameters [28] and have been widely studied [29,30] regardless of differences in device structures and fabrication techniques. Even though the effect of those parameters on the film microstructure and electronic property has been established by several groups [28,31], the detailed crystal nucleation and growth process of perovskite, after anti-solvent quenching and post-annealing, are still ambiguous. Careful inspection of the perovskite

crystal evolution can provide a simple way to modulate the perovskite growth to obtain high-quality perovskite film for efficient PSCs.

Herein, we presented an in-depth discussion of preparing highly efficient and reproducible TiO_2-NA PSCs with mixed-ion perovskite. In this work, the precursor-concentration dependent morphology and crystallization evolution of the corresponding mixed-ion perovskite films were carefully researched and modeled. Moreover, a detailed study has been carried out regarding the effects of crystallization evolution and film thickness on the electron collection, recombination, and photovoltaic performance. Combining the benefits of good crystallization of mixed-ion perovskite on TiO_2 NAs and high electron mobility of TiO_2 NAs, the PCEs of TiO_2-NA PSCs reached a great extent to a champion PCE of 19.33% with little hysteresis. A better performance can be expected by further optimizing the NAPSCs in the near future.

2. Experimental

2.1. Material synthesis

Titanium butoxide (97%, TBT), 2-ethyl-butyric acid (99%), formamidine acetate (99%), methylamine solution (33 wt% in methanol), hydroiodic acid (57 wt% in H_2O), lead bromide (PbBr$_2$, 99.999%), cesiumiodide (CsI, 99.9%), chlorobenzene (99.8%) and acetonitrile (99.8%) were purchased from Sigma-Aldrich. 2,2′,7,7′-tetrakis(N,N-di-p-methoxyphenylamine)-9,9′-spirobifluorene (Spiro-OMeTAD) was purchased from Lumtec (Taiwan). Lead (II) iodide (99.9985%) was purchased from Alfa Aesar. All other reagents and chemicals were purchased from Sinopharm Group Co. and used as received without any further purification.

2.1.1. Formamidinium iodide (NH = CHNH$_3$I, FAI).

Briefly, 5 g formamidine acetate was dissolved in 60 mL methanol in a round-bottomed flask immersed in an ice bath. Then, 10 mL hydroiodic acid (57 wt% in water) was dropped slowly into the round-bottomed flask. The solution was further stirred for 2 h at room temperature. The obtained light-yellow solution was then concentrated by rotary evaporation at 50 °C to obtain crude solids, which was then dissolved by a minimum amount of methanol, recrystallized in diethyl ether, and filtered. The dissolved and recrystallized procedures were repeated three times, and the resulting white solid was collected and dried at 60 °C under vacuum for 24 h.

2.1.2. Methylammonium bromide (CH$_3$NH$_3$Br, MABr)

Typically, 11.32 mL CH_3NH_2 solution was added into a round-bottomed flask immersed in an ice bath. Then, 14.67 mL hydrobromide acid (48 wt% in water) was dropped slowly into the round-bottomed flask. The crystallization and purification processes were similar to that of FAI.

2.1.3. TiO$_2$ NA

Fluorine-doped tin oxide (FTO) coated glasses (Grene, Qingdao, China) were cleaned with deionized water, acetone, and isopropanol, respectively. After drying, the FTO glasses were treated with UV-ozone for 15 min. A TiO_2 compact layer of 50 nm thickness was then prepared on the FTO surface. Briefly, a drop of

TBT/deionized water/HCl (37% in water) mixture (with a volume ratio of 74:1:1:1000) was spun on the FTO surface with 2000 rpm for 60 s, and further annealed at 450 °C for 60 min. Then, the FTO substrate with the compact TiO_2 layer was immersed in a Teflon-lined stainless-steel autoclave (25 mL) with 12 mL solution containing 2-ethyl-butyric acid/HCl/butanone (with a volume ratio of 2:4:6), and kept at 200 °C for 17 min [17]. Finally, the reactor was taken out from the oven and put into cold water immediately. After cooling down to room temperature, the TiO_2 NA-covered substrate was immersed in ethanol for 10 min and carefully washed with deionized water to remove the residues.

2.2. Solar cell fabrication

The PSCs with architecture of FTO/TiO_2 compact layer/TiO_2NA/mixed-ion perovskite/Spiro-OMeTAD/silver were prepared as presented in Fig. 1. The typical procedure is shown as below.

FAI, MABr, PbBr$_2$, and PbI$_2$ were added into a mixed solvent of DMFand DMSO (4:1 volume ratio) by a molar ratio of 1:0.2:0.2:1.1. Then CsI, pre-dissolved as a 1.5 M stock solution in DMSO, was added to the mixed DMF/DMSO solution to achieve the perovskite ($Cs_{0.1}(FA_{0.83}MA_{0.17})_{0.9}Pb(I_{0.83}Br_{0.17})_3$) precursor solution. The molar concentrations were fixed as 0.55 M, 0.80 M, 1.05 M, 1.30 M, and 1.55 M, respectively.

The deposition of the perovskite onto TiO_2NAs was performed in a nitrogen-filled glovebox by spin-coating at 1000 rpm for 10 s and then at 6000 rpm for 25 s. 200 μl chlorobenzene was poured on the spinning substrate at 3 s before the end of the procedure at the second spin-coating. The substrate was then heated at 100 °C for 60 min on a hot-plate. A hole-transport-layer solution was prepared by dissolving 72.3 mg Spiro-OMeTAD, 17.5 μL Li-bi s(trifluoromethanesulfonyl) imide (from a stock solution in 520 mg/mL in acetonitrile) and 28.8 μL tert-butylpyridine in 1 mL chlorobenzene. The Spiro-OMeTAD solution was subsequently spin-casted on top of the perovskite layer at 3000 rpm for 30 s. The devices were finalized by thermal evaporation of silver layers (100 nm thickness) on the top of Spiro-OMeTAD layers.

2.3. Characterization

The top-view and cross-section morphologies of the perovskite films were observed using a field-emission scanning electron microscope (SEM, SUPRA 55, Zeiss, Germany). X-ray diffraction (XRD) patterns of the perovskite films were recorded using a Rigaku Ultima-IV X-ray diffractometer. The absorption spectra were obtained by using a Shimadzu UV-2550 UV–vis spectrophotometer (Japan).

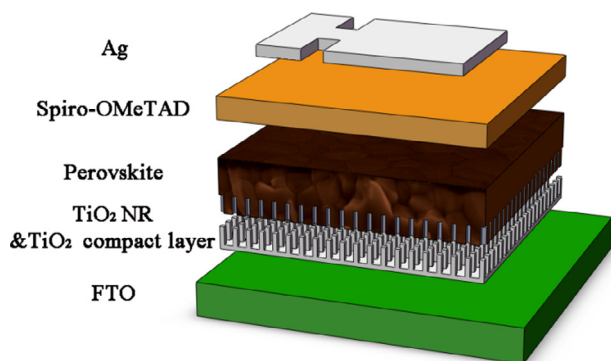The solar cells were measured using a 300 W xenon solar simulator (Newport Oriel Solar Simulators) with a source meter

(Keithley 2420, USA) under 100 mW/cm^2, AM 1.5G illumination, calibrated by a Si-reference cell. The J-V curves were scanned reversely from 1.2 V to −0.5 V, or forwardly from −0.5 V to 1.2 V. The step voltage was fixed at 100 mV. The active area for all devices was fixed by using a mask (0.06 cm^2). The external quantum efficiency (EQE) spectra were recorded using a solar cell quantum efficiency measurement system (QEX10, PV measurements, USA). Prior to the measurement, a standard silicon solar cell was used as the reference (012-2013, Pharos Technology).

Atomic force microscopy (AFM) images of the perovskite films on TiO_2NAs were tested using an in-ORCA mode with a bias of 0.6 V (Cypher S, Asylum Research, USA). Space-charge-limited current (SCLC) measurements were used to evaluate the electron mobility of the mixed-ion perovskite films with a source meter (Keithley 2420, USA). Time-resolved PL (TRPL) decay spectra of the perovskite/TiO_2 nanorods/compact TiO_2/FTO devices were measured by using an Edinburgh FLS 980-STM instrument (Livingston, WL, U.K.). Electrochemical impedance spectroscopy (EIS) measurements were made in the dark as a function of applied voltage from −0.75 V to −1.0 V on an electrochemical working station (CHI 660D, China). The FTO substrates were connected to the working electrode.

3. Results and discussion

3.1. Characterization of the perovskite films from different precursor solutions

The quality and morphology of the perovskite film are reported to be a critical issue for efficient PSCs [32]. To evaluate the effect of perovskite precursor concentrations (0.55 M, 0.80 M, 1.05 M, 1.30 M and 1.55 M) on the film morphology, top-view and cross-section-view images are given in Fig. 2.

As shown in Fig. 2, perovskite films composed of an infiltrated layer within the TiO_2 NA and an upper layer (the part over the top of the TiO_2 NA) are observed to crystallize on the TiO_2 NAs. The thickness of the upper layer increases with increasing the precursor concentration, ranging from 20-nm thick film from 0.55 M solution to 390-nm thick film from a 1.55 M solution (Fig. S1). Certain differences in the perovskite grain can also be observed between the samples from Fig. 2. Higher precursor concentration leads to larger grains. The statistics of the perovskite grain size derived from the obtained SEM images in Fig. 2 are shown in Fig. S2. The mean grain size of the perovskite film increases gradually from 88 to 260 nm when the concentration of solution is increased from 0.55 to 1.55 M. No doubt such difference comes from the precursor concentration difference. It is quite important to find out how the precursor concentration affects the crystallization of the perovskite, which is instructive for the preparation of high-quality perovskite film. Considering the film-preparation process, two stages can be divided as a quenching stage and the annealing stage. Perovskite crystallites along with intermediate-phase complex, MA(FA)I(Br)-PbI$_2$-DMSO, are formed at the first stage. At the second annealing stage, all the intermediate-phase complexes turn into perovskite phase and all the perovskite crystallites grow up to some extent [33]. Actually, the second stage belongs to the Ostwald ripening process [34], for which the driving force is the well-known curvature dependence of the atoms' diffusion between different-sized grains [35]. To determine which stage is the key process responsible for the crystallization difference, further characterization is required.

Hence, the SEM images of the surface morphology and the cross section morphology of the five as-quenched films are presented in Fig. 3. The statistics of the grain size derived from the obtained SEM images in Fig. 3 are shown in Fig. S3. The mean grain size of
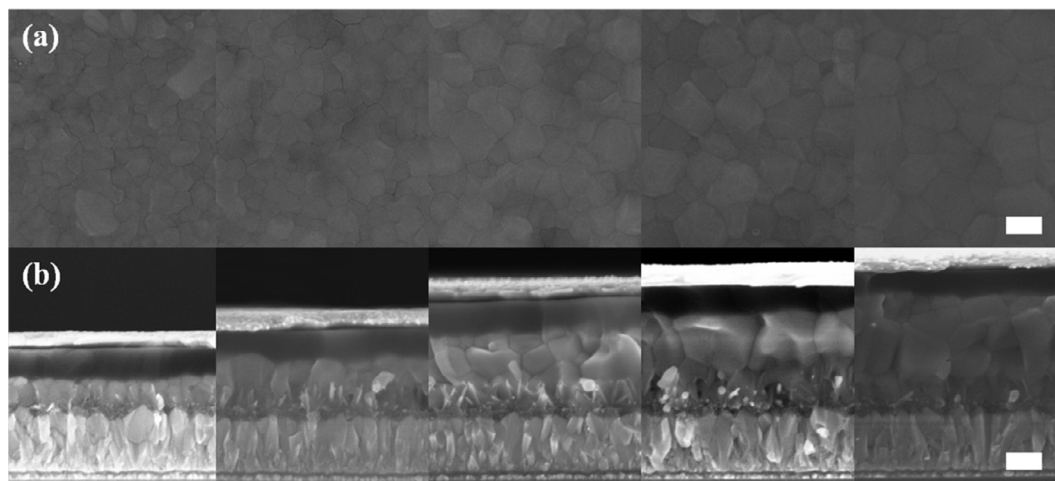

Fig. 1. Schematic of aperovskite solar cell based on TiO_2 NA.

Fig. 2. The representative (a) morphology and (b) cross section morphology of PSCs with different perovskite precursor concentrations. As shown in (b), the configuration of all the PSCs is FTO/TiO$_2$ compact layer/TiO2 NA/Perovskite/Spiro–OMeTAD/Ag from down to top. The scale bar is 200 nm.
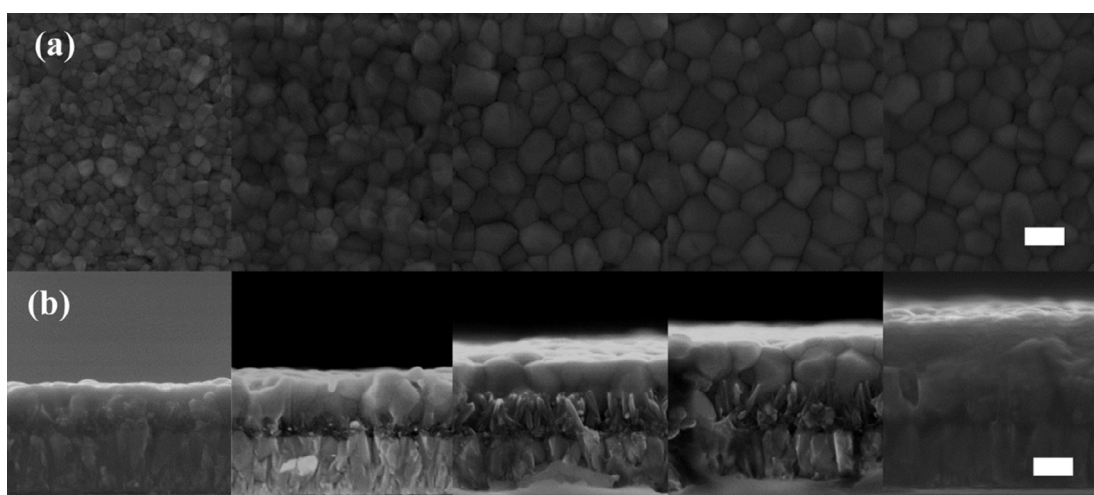

Fig. 3. The surface morphology and cross-section morphology of the as-quenched perovskite films from different precursor concentrations (0.55 M, 0.80 M, 1.05 M, 1.30 M, 1.55 M), respectively. The scale bar is 200 nm.

the five as-quenched films increases gradually from 75 to 181 nm when the concentration of the solution is increased from 0.55 to 1.55 M. Compared with the results in Fig. S2, it is assured that different grain morphologies would come into being at the quenching stage. Meanwhile, a slight increase of the perovskite grain size can also be observed at the second annealing stage for all samples. Overall, it can preliminarily concluded that the first quenching stage has much more effect on the crystallite difference.

X-ray diffraction (XRD) measurements were also performed to investigate the crystal structure difference of the five as-quenched films, as shown in Fig. 4. All the XRD patterns contain several intensive peaks, belonging to the FTO, composite perovskite, and an intermediate product. The XRD pattern of the TiO$_2$ NA/FTO is presented in Fig. S4. The weak peaks, locating at ~26.8° and ~38.2° in Fig. 4, are attributed to FTO [17], and the feature peaks of TiO$_2$ are too weak to be observed. Featuring diffraction peaks owing to the trigonal perovskite phase (P3m1) can be seen from all patterns [36]. Moreover, the peak at ~9.2° belongs to the intermediate product, MA(FA)I(Br)-PbI$_2$-DMSO complex [33]. It can be concluded that perovskite crystallites coexist with some intermediate phase after anti-solvent quenching. Herein, the representative (1 0 1) facet was used to compare the perovskite

crystal size [28]. The calculated crystal size was listed in Table S1 based on Scherrer equation. Obviously, the crystal size increases with increasing the precursor concentration, which also implies a faster crystallization in the low precursor concentration samples. The result agrees well with the SEM result.

According to the SEM and XRD results, it can be inferred that the crystallite difference comes into being, owing to different solvent extraction speeds from those wet perovskite films, at the first quenching stage. When the chlorobenzene anti-solvent was poured on the spinning wet perovskite film, the surface solvent molecules will be extracted immediately. A uniform and dense thin perovskite layer, named capping layer in this context, will form on the surface simultaneously, shown in Fig. 5(a). Then the extraction of solvent molecules under the uniform layer will be hindered greatly. A thicker wet film gives a slower extraction speed. As illustrated in Fig. 5(b) and (c), more solvent molecules will be left within the thicker wet films logically. Though the thinner film is from lower concentrated perovskite precursor solution, the concentration of the solution under the capping layer is higher than those of its counterparts. We named this concentration conversion as a result of "capping effect". Furthermore, more solvent residues might lead to more intermediate phases, as proven in Fig. 4.
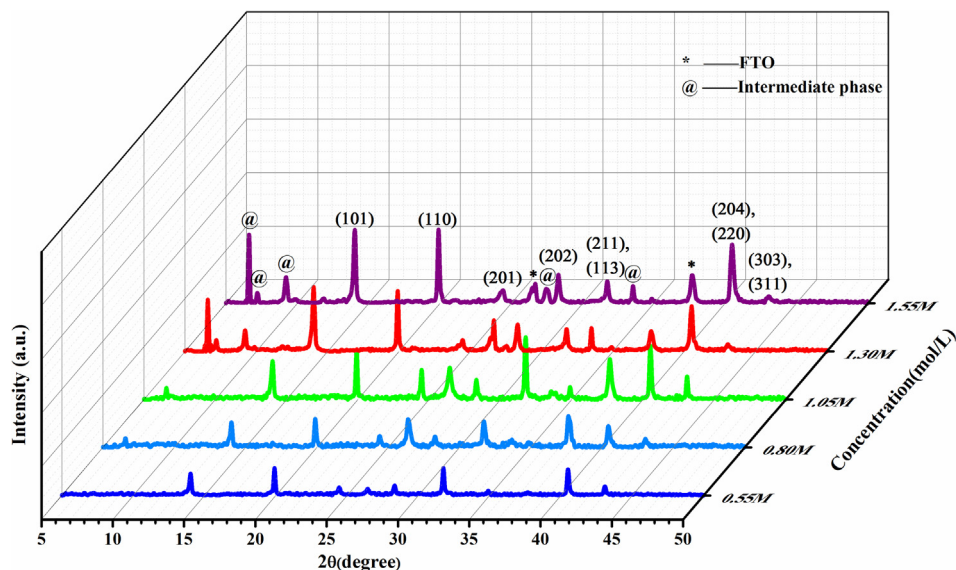
Fig. 4. The XRD patterns of the as-quenched perovskite films from different perovskite precursor concentrations.
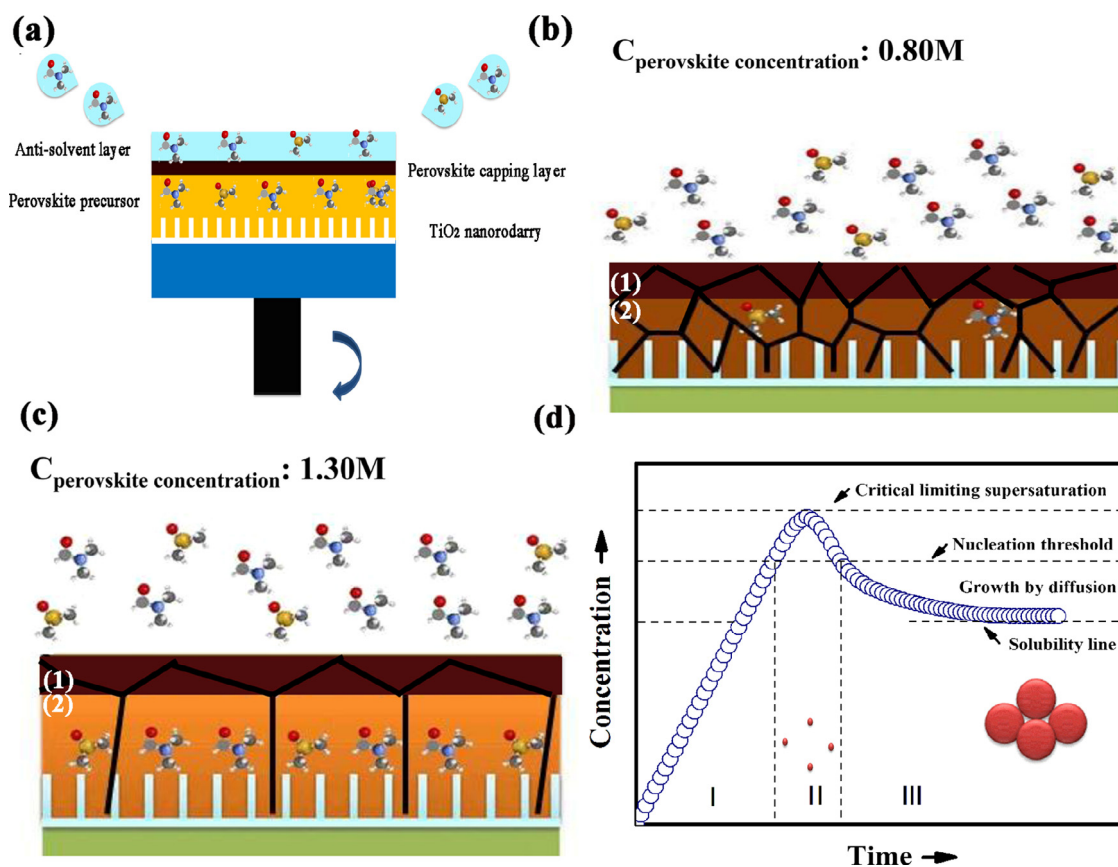

Fig. 5. The schematic of (a) the solvent extraction when chlorobenzene is poured down, the forming capping layer (1) with perovskite solution (2) beneath on (b) a thinner wet perovskite film and (c) a thicker perovskite wet film. Solvent molecules exist both within the film and on the surface; (d) LaMer Model for the nucleation and growth of crystals in mother solution.

With the further evaporation of solvent molecules after quenching, the nucleation process begins, which follows a LaMer theory, underneath the capping layer [37]. The LaMer model, shown in Fig. 5(d), is used widely for the explanation of most crystal nucleation and growth process from liquid solutions. In LaMer model, when the precursor solution reaches a critical concentration, many nucleuses come into being simultaneously and start to grow (Stage I). However, with the continuous consumption of the solute for the crystal nucleation and growth, the solution concentration will decrease to some extent and then the nucleation will be stopped (Stage II). Finally, there is only the growth of the crystals (Stage III). For the thinner wet perovskite film, the solution underneath

the capping layer has a higher concentration, because of the capping effect, and reaches the threshold crystallized concentration faster. As a result, large number of smaller crystallites are produced based on LaMer theory. On the contrary, lager crystals can be obtained on the thicker films from perovskite precursor solutions with higher concentrations. Wang has observed similar phenomena [38]. By the way, if none of anti-solvent quenching is applied, the solvent from the wet film will evaporate freely and lead to a porous and non-uniform film, as shown in Fig. S5.

Actually, the capping effect is beneficial for the preparation of high-quality perovskite film. For example, Zou et al. have used a heterogeneous cap or homogeneous cap for a slower evaporation of solvent molecules within the perovskite films to deliver large-size perovskite grains [39–41]. According to our analysis and our experience, the quenching time and controlling the extraction of solvent molecules within the wet perovskite film are extremely important for high-quality perovskite films with large grain sizes [39].

Post-annealing treatment was used to further remove residue solvents within the quenched films. During that stage, all the samples go through a crystal growth and coalescence process. In order to get further insight into the effect of post-annealing treatment, the crystal structures of the samples were also investigated with XRD, as shown in Fig. 6. It can be seen that there are two peaks at ~12.7° at the patterns of the perovskite films from concentrations of 0.55 M and 0.80 M. The two peaks belong to the featuring peak of PbI_2 (0 0 1). The previous study on the interfacial structure of perovskite/TiO_2 has shown a spectroscopic evidence for the presence of PbI_2 and methylamine as well when a thin perovskite-layer was coated on the TiO_2 surface [42]. TiO_2 is assumed to account for the existence of PbI_2 by decomposing the perovskite at the interface. The role of PbI_2 is suggested to be either positive [43] or negative [44] for the photovoltaic performance, which depends on different conditions. As the precursor concentration is increased, the featuring peak of PbI_2 residues disappear.

More importantly, the peak intensities of (1 0 1)/(2 0 2)/(3 0 3) facets are increased compared with those of the (1 1 0)/(2 2 0) facets. Herein, we selected the representative facets (1 0 1) and (1 1 0) to investigate the crystal growth process. The intensity ratio is calculated and shown in Fig. S6. It can be seen that the intensity ratio of (1 0 1)/(1 1 0) facet shows a slightly increasing tendency with the increased precursor concentration for those as-

quenched samples, which is likely contrary to the LaMer theory. The capping effect of the fastest formed perovskite layer might lead to such result as discussed above. With further post-annealing, the residue solvents can be evaporated from the films. The increased (1 0 1) facets of the films from high precursor concentrations indicate better perovskite phase in cases of the higher precursor concentrations. The previous study reported that the increased peak intensity of (1 0 1) facet would be beneficial for the electron injection at the interface of perovskite/TiO_2 [31], and their photovoltaic performance. Meanwhile, the crystal size along with the normal direction of (1 0 1) facet was calculated with Scherrer equation again to evaluate the growth of the crystals during the Ostwald ripening process, as shown in Table S1. It can be seen that the average crystal growth rate of five films during annealing treatment are basically the same, around 0.14 nm/min, which proves that the difference of the five films is mainly formed at the quenching stage.

3.2. Photovoltaic performance of the different perovskite films

Since perovskite films with different grain sizes have been obtained, their impact on the photovoltaic performance was evaluated. The typical device structures can be seen in Fig. 1. The average photovoltaic parameters with standard deviation are listed in Table 1.

As shown in Table 1, the increased precursor concentration, from 0.55 M to 1.30 M, leads to the increase of average short-circuit current density (J_{sc}) from 16.24 ± 0.54 mA/cm^2 to 23.16 ± 0.60 mA/cm^2. The increase of J_{sc} is mainly due to the increased light absorption, as shown in Fig. S7. Further increasing the precursor concentration decreases the average J_{sc} to 21.85 ± 0.95 mA/cm^2, corresponding to 5.7% decrement. The average open-circuit voltage (V_{oc}) shows a similar tendency to the average short-circuit current density (J_{sc}), from 0.55 M to 1.30 M, enhanced from 0.960 ± 0.021 to 1.131 ± 0.013 V, but slightly declines to 1.123 ± 0.018 V when the precursor concentration is 1.55 M. The fill factor (FF) also shows a similar change tendency to those of J_{sc} and V_{oc}. FF is improved gradually from 0.662 ± 0.003 to 0.714 ± 0.015, from 0.55 M to 1.30 M. Higher precursor concentration (1.55 M) decreases the FF to 0.706 ± 0.03. Considering the change of J_{sc}, V_{oc}, and FF, the optimal precursor concentration for the high photovoltaic performance of these solar cells should be 1.30 M, exhibiting the highest average power conversion efficiency
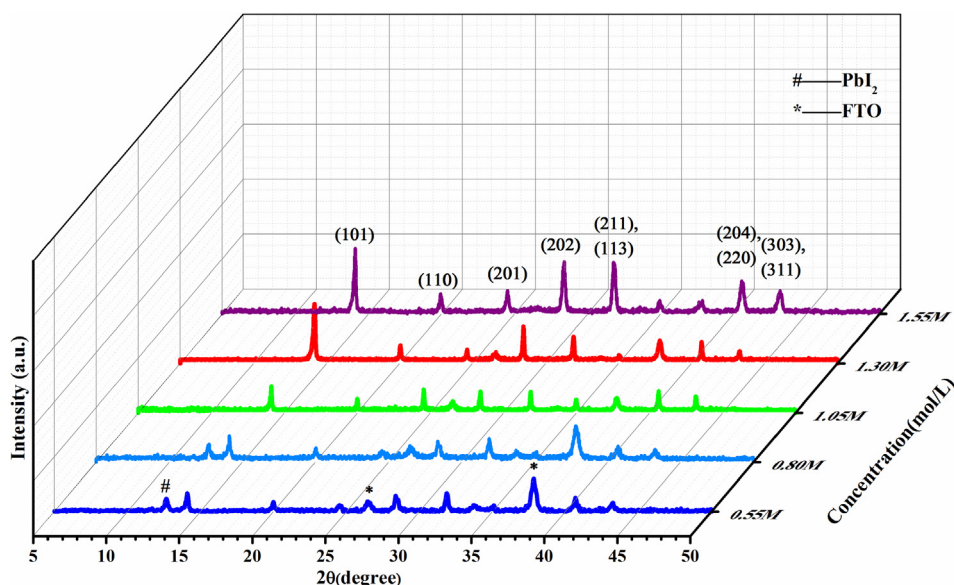

Fig. 6. The XRD patterns of the post-annealed perovskite films from different perovskite precursor concentrations.

Table 1
Photovoltaic Parameters with standard deviation of Short-Circuit Photocurrent Density (J_{sc}), Open-Circuit Voltage (V_{oc}), Fill Factor (FF), and Power Conversion Efficiency (PCE) of the perovskite solar cells evolved with perovskite precursor concentrations.

Perovskite concentration (mol/L)	V_{oc} (V)	J_{sc} (mA/cm^2)	FF	PCE(%)
0.55	0.960 ± 0.021	16.24 ± 0.54	0.662 ± 0.003	10.32 ± 0.47
0.80	1.011 ± 0.023	17.91 ± 0.82	0.665 ± 0.013	12.04 ± 0.65
1.05	1.096 ± 0.032	19.38 ± 0.74	0.671 ± 0.022	14.25 ± 1.07
1.30	1.131 ± 0.013	23.16 ± 0.60	0.714 ± 0.015	18.69 ± 0.47
1.55	1.123 ± 0.018	21.85 ± 0.95	0.706 ± 0.03	17.32 ± 0.70

of 18.69%. For comparison, a device with a non-quenching perovskite film (1.30 M) was also prepared and gave a poor efficiency of 6.3%, shown in Fig. S8, which is owing to the low-quality perovskite shown in Fig. S5.

J-V curves of one of the highest-performing devices under different scan directions under one Sun (AM 1.5) are presented in Fig. 7(a). In the reverse scan, the device generates a J_{sc} of 23.53 mA/cm^2, a V_{oc} of 1.149 V, and an FF of 0.715, which yields a PCE of 19.33%. To the best of our knowledge, this is the highest PCE reported, by far, among the one-dimensional array-based hybrid inorganic-organic solar cells. In addition, the PCE obtained from the forward scan (18.81%) was close to that from reverse scan indicating a negligible J-V hysteresis for this kind of cells. Meanwhile, we measured EQE to verify our measured Jsc. The EQE is the percentage of collected electrons, obtained under short circuit current conditions, related to the number of incident photons and can be used to determine the contribution of the photons of different energy to the charge generation in the solar cells. The spectral response of the champion solar cell is shown in Fig. 7 (b), which yields an integrated J_{sc} of 22.85 mA/cm^2.

Furthermore, good stability can be achieved on the champion device. The output of J_{sc} and PCE at the maximum power point was recorded at a bias voltage of 0.91 V, as shown in Fig. S9. The J_{sc} was stabilized at 21.1 mA cm^{-2} and the PCE was stabilized at 19.2% for about 200 s. The PCE of the device remained above 96% of the initial value after 1000-hour atmospheric storage (humidity lower than 10% in electronic box), as shown in Fig. S10. Even though the humidity level is somewhat low and not comparable to the real environment, the TiO$_2$ NA based device shows its great potential in the stability aspect. Compared with its counterpart, nanoparticle based film, the TiO$_2$ NA structure possesses unique highly-ordered 1D architecture which can remarkably protect the perovskite from the moisture expected from the hole transport layer side. With further sealing to reduce the attack of moisture from the hole transport layer side or the grain-boundary engineer-

ing of perovskite films, outstanding stability can be achieved on the TiO$_2$-NAPSCs.

3.3. Inspection of charge transport and recombination within the different perovskite films

As discussed above, the combined effect of perovskite precursor concentration on J_{sc}, V_{oc} and FF resulted in an improved efficient PSCs when the optimal precursor concentration was 1.30 M. Considering the same TiO$_2$ NA based photoanodes, hole transport material and Ag metal electrode are applied for all the devices, the improved photovoltaic performance of PSCs might also come from the modified perovskite/TiO$_2$NA interface and the electron transport within the perovskite layer, besides the light absorption difference. To explore the effect of precursor concentration on the perovskite/TiO$_2$ NA interface, time-resolved photoluminescence (TRPL) decay measurements are used. Transient photoluminescence (PL) profiles for perovskite thin films evolved with different precursor concentrations on FTO/compact TiO$_2$/TiO$_2$ NA are exhibited in Fig. 8.

The PL lifetime can be fitted by a bi-exponential decay function:

$$I(t) = A1 \exp(-t/\tau_1) + A2\exp(-t/\tau_2) \tag{1}$$

where the fast decay lifetime τ_1 can be ascribed to the quenching of free carriers from perovskite crystals to TiO$_2$ NAs and the slow decay process τ_2 is related to the radiative decay in perovskite polycrystalline film [45]. The detailed data is given in Table S2. Aiming at the inspection of varied charge transfer between TiO$_2$ NA and perovskite layer, only the change of the fast decay lifetime is discussed here. When the precursor concentration is as low as 0.55 M, the fastest decay lifetime τ_1, 2.90 ns, is obtained. With the increase of perovskite precursor concentration, τ_1 increases first, 5.31 ns (0.80 M), 8.79 ns (1.05 M) and then decreases gradually to 5.50 ns (1.30 M), and to 2.96 ns (1.55 M), respectively. The overall change of the electron-extraction lifetime from perovskite film to
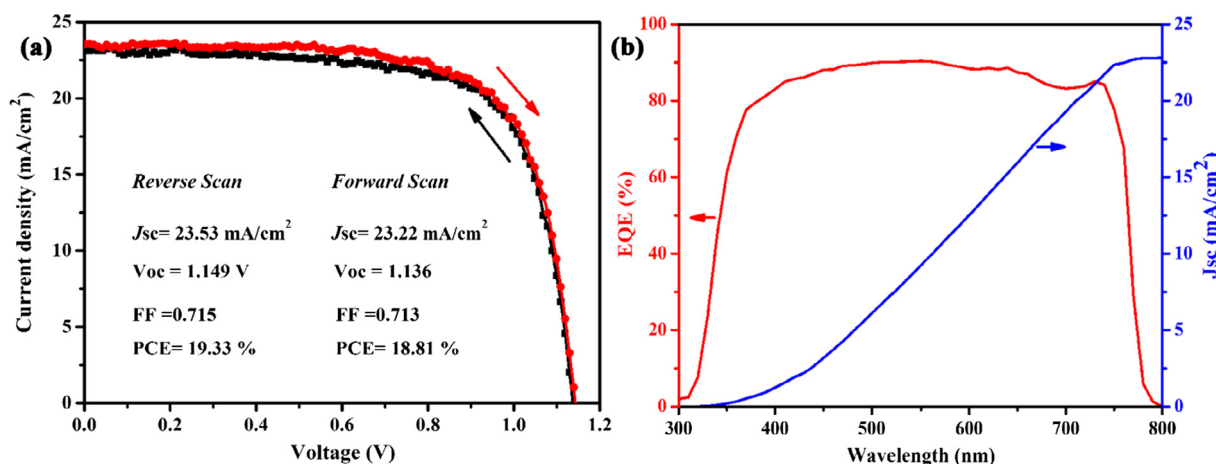

Fig. 7. (a) Current-voltage characteristics on the perovskite solar cells with a starting perovskite precursor solution of 1.30 M under AM1.5G one sun illumination and (b) spectral response of the champion solar cell.
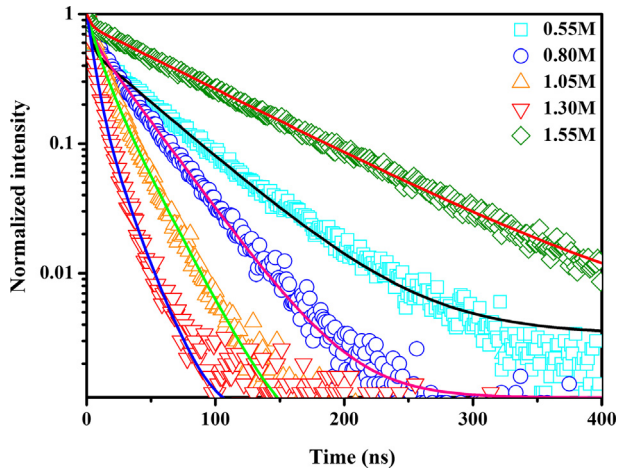
Fig. 8. Time-resolved PL spectra of the perovskite films on FTO/compact TiO$_2$ layer/ TiO$_2$NAs prepared using different perovskite precursor solutions.

TiO$_2$ is similar to the trend of grain size change. It might be inferred that the fewer grain boundaries between perovskite crystals and TiO$_2$ NAs has a positive effect on the charge extraction [21]. Also, the decreased bulk traps of larger grains around TiO$_2$ NAs will reduce the trapped electrons[22]. Space-charge-limited current (SCLC) method was performed to determine the electron mobility of the perovskite films. Devices, with architectures of FTO/TiO$_2$ NA/perovskite film/PCBM/Au, were fabricated and measured, as shown in Fig. S11. The ohmic regime and SCLC regime are found at low voltages and at high voltages, respectively [39]. By using the Mott-Geurst's SCLC model and a trap-filled model, the electron mobility and the trap density can be obtained. The increased precursor concentration leads to the increase of electron mobility from 4.78E to 04 to 4.66E−03, 1.82 E−02, 2.75 E−02, and 3.03 E−02 cm^2 V^{-1} S^{-1} for 0.55-M, 0.80-M, 1.05-M, 1.30-M and 1.55-M precursors, respectively. Meanwhile, the trap density decreases from 5.23 E+16 to 3.69 E+16, 3.40 E+16, 3.21 E+16 and 3.02 E+16 with the increased precursor concentrations, respectively. Obviously, the increased electron mobility and the decreased trap density with the increased precursor concentration profit from the increased grain size.

Though the larger grains have fewer defects and traps, over-large grains might lead to over-thick film and longer diffusion way of photon-induced electrons. As for the perovskite film from the 1.55 M precursor solution, the weight fraction of the slow decay process increases to 99%, indicating a dominating mechanism of radiative decay. Hence, the perovskite film prepared from

the 1.30 M precursor solution exhibited the highest charge-dissociation efficiency, with a high weight fraction of the decreased fast decay lifetime. The observed high average J$_{sc}$ (23.16 mA/cm^2) and average FF (0.714) of the devices derived from the 1.30 M precursor solution might be attributed to this efficient charge separation and collection. To further study the effect of larger grain size accompanied by the thicker film on the photon-induced electron transportation and recombination, conductive atomic force microscopy (c-AFM) analyses were carried out to measure the local current distribution over the perovskite films. To fully evaluate the electron transport through grains and grain boundaries, a bias voltage of 0.5 V was adopted during the c-AFM measurement process. [46] Perovskite/TiO$_2$ NA/TiO$_2$ compact layer/FTO devices (1.30 M and 1.55 M) were used in the c-AFM measurement. The topography and corresponding current mapping are presented in Fig. 9.

Together with the results in Fig. 2, it is found that all the perovskite films (1.30-M, and 1.55-M based) consisting of both large grains and small grains have a relatively rougher surface. The previous report indicated that, at a high positive bias voltage, the grain boundaries would act as channels for current to flow rather than recombination sites [47]. As can be seen in Fig. 9(a), at the positive bias voltage, a positive current flows through the gains and the grain boundaries uniformly with an average magnitude of 208 pA for the perovskite film from 1.30 M precursor. In addition, the dark area in Fig. 9(a) may be ascribed to the impurity phases [47], generated during the preparation process or the c-AFM measurement in an air atmosphere. In contrast, a lower current passing through the perovskite film from higher precursor concentration (1.55 M) with an average magnitude of 175 pA is observed in Fig. 9(b). It can be deduced that the lowering current might come from the increasing recombination during the transport process from the top of perovskite film to the FTO substrate. Though there are fewer defects for each larger perovskite crystal grain in the perovskite film (1.55 M), the film is thicker resulting in a longer transport way and increased total recombination sites. The crystalline grain size and the thickness of the perovskite film have a bifacial effect on the performance of the PSCs. These results further demonstrate the results above.

Electronic impedance spectroscopy measurement was performed to determine the interfacial charge recombination dynamics of different devices. Fig. 10(a) presents the typical corresponding Nyquist plots for those devices at a bias of −0.8 V. Two separated semicircles can be found in the plots, from which recombination resistance within the perovskite films and their interfaces can be fitted from the plots. Fig. 10(b) compares the interfacial charge recombination resistance (R$_{re}$) between perovskite and its contacts in the devices at varied bias, indicating that R$_{re}$ for device from 1.3 M is always larger than those of other devices. On the
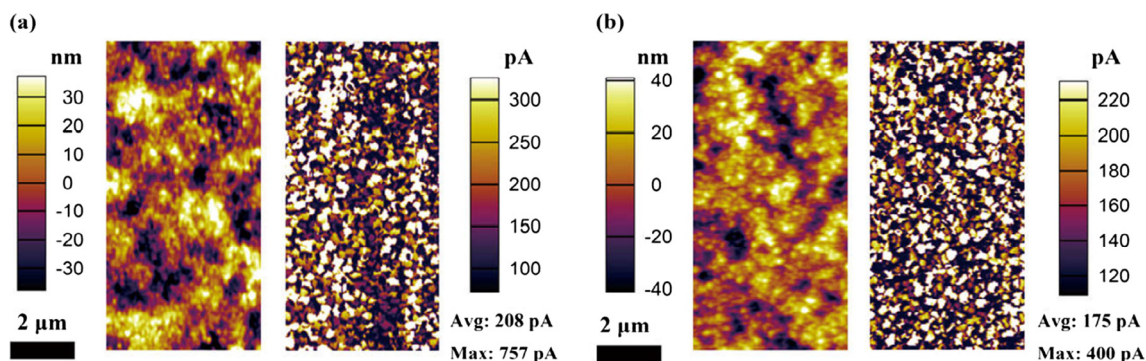

Fig. 9. Topographic images and corresponding current images of (a) a perovskite (1.30 M) /TiO$_2$ NA/c-TiO$_2$/FTO and (b) a perovskite (1.55 M) /TiO$_2$ NA/c-TiO$_2$/FTO typical devices.
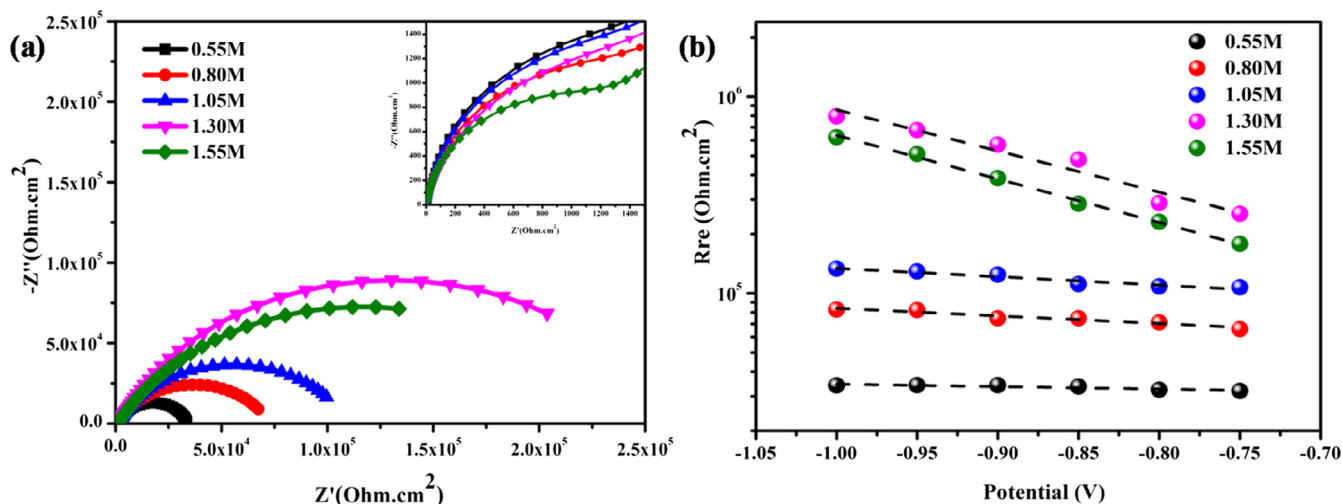
Fig. 10. (a) Typical Nyquist plots of the devices from different concentrated perovskite precursor solutions in the dark. The frequency range is from 1 MHz to 0.1 Hz; the bias is −0.8 V. (b) Interfacial recombination resistance (R_{re}) extracted from the Nyquist plots of the devices from different concentrated perovskite precursor solutionsrecorded at different biases in the dark.

other word, the device with the perovskite film from 1.30 M precursor solution shows much decreased interfacial recombination, which agrees well with AFM results and IV results. The suppressed interfacial charge recombination could be owing to a balance of the larger crystallite size and the film thickness. This is further confirmed with the transient decay measurements in Fig. 8.

4. Conclusions

To sum up, the effect of precursor concentration on the crystallization and photovoltaic performance of mixed-ion perovskite films for PSCs based on TiO₂ NAs has been studied. First, higher precursor concentration was found to be favorable for the formation of larger perovskite crystallites via anti-solvent quenching method. A detailed inspection of the as-quenched perovskite films revealed that the quenching changed the evaporation of the solvent molecules from the wet perovskite film and was mainly responsible for differed nucleation and growth of the perovskite crystallites. It is the first time to disclose the relationship between the precursor concentration and the final perovskite crystal features in the case of anti-solvent quenching. Second, photovoltaic characterizations showed that thicker perovskite film with larger crystallites was beneficial for highly-efficient TiO₂-NA based PSCs. SCLC measurements and time-resolved PL measurements indicated that larger crystallites had lower trap densities and were good for photoinduced electron transport and extraction. However, PL measurements and EIS characterizations showed that the recombination within the perovskite was increased when the film thickness was a bit too thick. Finally, perovskite precursor solution with a concentration of 1.30 M was suitable for highly efficient and hysteresis-free PSCs with a champion PCE of 19.33%. Our results are believed to be very instructive for the fabrication of high quality perovskite films using anti-solvent quenching method. The key point is to avoid too fast nucleation process at the quenching stage by optimizing the precursor concentration, spin-coating parameters, and quenching time. Further investigation on the TiO₂ NA based perovskite solar cells could be turned to the practical long-term stability.

Acknowledgements

Appendix A. Supplementary material

Supplementary data to this article can be found online at https://doi.org/10.1016/j.jcis.2018.09.045.

References

[1] A. Kojima, K. Teshima, Y. Shirai, T. Miyasaka, Organometal halide perovskites as visible-light sensitizers for photovoltaic cells, J. Am. Chem. Soc. 131 (17) (2009) 6050–6051.
[2] P. Gao, M. Gratzel, M.K. Nazeeruddin, Organohalide lead perovskites for photovoltaic applications, Energy Environ. Sci. 7 (8) (2014) 2448–2463.
[3] C. Jin, Y. Huailiang, L. Junpeng, X. Xiaobao, S. Yan, L. Hong, W. Mingkui, Recent progress in efficient hybrid lead halide perovskite solar cells, Sci. Technol. Adv. Mater. 16 (3) (2015) 036004.
[4] W. Chen, Y. Wu, Y. Yue, J. Liu, W. Zhang, X. Yang, H. Chen, E. Bi, I. Ashraful, M. Gratzel, L. Han, Efficient and stable large-area perovskite solar cells with inorganic charge extraction layers, Science 350 (6263) (2015) 944.
[5] W.S. Yang, B.-W. Park, E.H. Jung, N.J. Jeon, Y.C. Kim, D.U. Lee, S.S. Shin, J. Seo, E. K. Kim, J.H. Noh, S.I. Seok, Iodide management in formamidinium-lead-halide-based perovskite layers for efficient solar cells, Science 356 (6345) (2017) 1376.
[6] N.G. Park, Perovskite solar cells: an emerging photovoltaic technology, Mater. Today 18 (2) (2015) 65–72.
[7] N.S. Marinova, Valero, J.L. Delgado, Organic and perovskite solar cells: working principles, materials and interfaces, J. Colloid Interface Sci. 488 (2017) 373.
[8] P.A. Bouit, F. Spänig, G. Kuzmanich, E. Krokos, C. Oelsner, M.A. Garcia-Garibay, J.L. Delgado, N. Martin, D.M. Guldi, Efficient utilization of higher-lying excited states to trigger charge-transfer events, Chem.-A Eur. J. 16 (31) (2010) 9638–9645.
[9] H. Tan, A. Jain, O. Voznyy, X. Lan, F.P. Garcia de Arquer, J.Z. Fan, R. Quintero-Bermudez, M. Yuan, B. Zhang, Y. Zhao, F. Fan, P. Li, L.N. Quan, Y. Zhao, Z.-H. Lu, Z. Yang, S. Hoogland, E.H. Sargent, Efficient and stable solution-processed planar perovskite solar cells via contact passivation, Science 355 (6326) (2017) 722.
[10] H.-S. Kim, J.-W. Lee, N. Yantara, P.P. Boix, S.A. Kulkarni, S. Mhaisalkar, M. Gratzel, N.-G. Park, High Efficiency solid-state sensitized solar cell-based on submicrometer rutile TiO₂ nanorod and CH₃NH₃PbI₃ perovskite sensitizer, Nano Lett. 13 (6) (2013) 2412–2417.
[11] P. Qin, M. Paulose, M.I. Dar, T. Moehl, N. Arora, P. Gao, K. Varghese Ooman, M. Gratzel, K. Nazeeruddin Mohammad, Stable and efficient perovskite solar cells based on titania nanotube arrays, Small 11 (41) (2015) 5533–5539.

[12] H. Aibin, Z. Jingting, Z. Jianyun, Y. Yu, L. Yan, Y. Songwang, B. Shanhu, L. Lei, J. Ping, Mesostructured perovskite solar cells based on highly ordered TiO$_2$ network scaffold via anodization of Ti thin film, Nanotechnology 28 (5) (2017) 055403.

[13] A. Fakharuddin, F. Di Giacomo, A.L. Palma, F. Matteocci, I. Ahmed, S. Razza, A. D'Epifanio, S. Licoccia, J. Ismail, A. Di Carlo, T.M. Brown, R. Jose, Vertical TiO$_2$ nanorods as a medium for stable and high-efficiency perovskite solar modules, ACS Nano 9 (8) (2015) 8420–8429.

[14] Y.-N. Zhang, B. Li, L.-Y. Zhang, L.-W. Yin, Efficient electron transfer layer based on Al$_2$O$_3$ passivated TiO$_2$ nanorod arrays for high performance evaporation-route deposited FAPbI$_3$ perovskite solar cells, Sol. Energy Mater. Sol. Cells 170 (2017) 187–196.

[15] S.S. Mali, C.A. Betty, P.S. Patil, C.K. Hong, Synthesis of a nanostructured rutile TiO$_2$ electron transporting layer via an etching process for efficient perovskite solar cells: impact of the structural and crystalline properties of TiO$_2$, J. Mater. Chem. A 5 (24) (2017) 12340–12353.

[16] M. Salado, M. Oliva-Ramirez, S. Kazim, A.N.R. Gonzez-Elipe, S. Ahmad, 1-dimensional TiO$_2$ nano-forests as photoanodes for efficient and stable perovskite solar cells fabrication, Nano Energy 35 (2017) 215–222.

[17] X. Li, S.-M. Dai, P. Zhu, L.-L. Deng, S.-Y. Xie, Q. Cui, H. Chen, N. Wang, H. Lin, Efficient perovskite solar cells depending on TiO$_2$ nanorod arrays, ACS Appl. Mater. Interfaces 8 (33) (2016) 21358–21365.

[18] C. Gao, S. Yuan, B. Cao, J. Yu, SnO$_2$ nanotube arrays grown via an in situ template-etching strategy for effective and stable perovskite solar cells, Chem. Eng. J. 325 (2017) 378–385.

[19] Y.-Z. Zheng, E.-F. Zhao, F.-L. Meng, X.-S. Lai, X.-M. Dong, J.-J. Wu, X. Tao, Iodine-doped ZnO nanopillar arrays for perovskite solar cells with high efficiency up to 18.24%, J. Mater. Chem. A 5 (24) (2017) 12416–12425.

[20] S. Zihang, T. Guoqing, L. Huan, L. Guopeng, M. Shuai, Y. Shimeng, L. Qian, J. Yang, Three-dimensional architecture hybrid perovskite solar cells using CdS nanorod arrays as an electron transport layer, Nanotechnology 29 (2) (2018) 025401.

[21] C. Liu, R. Zhu, A. Ng, Z. Ren, S.H. Cheung, L. Du, S.K. So, J.A. Zapien, A.B. Djurisic, D. Lee Phillips, C. Surya, Investigation of high performance TiO$_2$ nanorod array perovskite solar cells, J. Mater. Chem. A 5 (30) (2017) 15970–15980.

[22] B. Conings, J. Drijkoningen, N. Gauquelin, A. Babayigit, J. D'Haen, L. D'Olieslaeger, A. Ethirajan, J. Verbeeck, J. Manca, E. Mosconi, D. Angelis Filippo, H.G. Boyen, Intrinsic thermal instability of methylammonium lead trihalide perovskite, Adv. Energy Mater. 5 (15) (2015) 1500477.

[23] R.K. Misra, S. Aharon, B. Li, D. Mogilyansky, I. Visoly-Fisher, L. Etgar, E.A. Katz, Temperature- and component-dependent degradation of perovskite photovoltaic materials under concentrated sunlight, J. Phys. Chem. Lett. 6 (3) (2015) 326–330.

[24] C.C. Stoumpos, C.D. Malliakas, M.G. Kanatzidis, Semiconducting tin and lead iodide perovskites with organic cations: phase transitions, high mobilities, and near-infrared photoluminescent properties, Inorg. Chem. 52 (15) (2013) 9019–9038.

[25] T. Jesper Jacobsson, J.-P. Correa-Baena, M. Pazoki, M. Saliba, K. Schenk, M. Gratzel, A. Hagfeldt, Exploration of the compositional space for mixed lead halogen perovskites for high efficiency solar cells, Energy Environ. Sci. 9 (5) (2016) 1706–1724.

[26] M. Saliba, T. Matsui, J.-Y. Seo, K. Domanski, J.-P. Correa-Baena, M.K. Nazeeruddin, S.M. Zakeeruddin, W. Tress, A. Abate, A. Hagfeldt, M. Gratzel, Cesium-containing triple cation perovskite solar cells: improved stability, reproducibility and high efficiency, Energy Environ. Sci. 9 (6) (2016) 1989–1997.

[27] M. Saliba, T. Matsui, K. Domanski, J.-Y. Seo, A. Ummadisingu, S.M. Zakeeruddin, J.-P. Correa-Baena, W.R. Tress, A. Abate, A. Hagfeldt, M. Gratzel, Incorporation of rubidium cations into perovskite solar cells improves photovoltaic performance, Science 354 (6309) (2016) 206.

[28] D. Bi, J. Luo, F. Zhang, A. Magrez, N. Athanasopoulou Evangelia, A. Hagfeldt, M. Gratzel, Morphology engineering: a route to highly reproducible and high efficiency perovskite solar cells, ChemSusChem 10 (7) (2016) 1624–1630.

[29] D. Bi, A.M. El-Zohry, A. Hagfeldt, G. Boschloo, Unraveling the effect of PbI$_2$ concentration on charge recombination kinetics in perovskite solar cells, ACS Photonics 2 (5) (2015) 589–594.

[30] A. Dualeh, N. Titreault, T. Moehl, P. Gao, K. Nazeeruddin Mohammad, M. Gratzel, Effect of annealing temperature on film morphology of organic-inorganic hybrid perovskite solid-state solar cells, Adv. Funct. Mater. 24 (21) (2014) 3250–3258.

[31] B. Zhang, M.-J. Zhang, S.-P. Pang, C.-S. Huang, Z.-M. Zhou, D. Wang, N. Wang, G.-L. Cui, Carrier transport in CH$_3$NH$_3$PbI$_3$ films with different thickness for perovskite solar cells, Adv. Mater. Interfaces 3 (17) (2016) 1600327.

[32] E. Eperon Giles, M. Burlakov Victor, P. Docampo, A. Goriely, J. Snaith Henry, Morphological control for high performance, solution-processed planar heterojunction perovskite solar cells, Adv. Funct. Mater. 24 (1) (2013) 151–157.

[33] N.J. Jeon, J.H. Noh, Y.C. Kim, W.S. Yang, S. Ryu, S.I. Seok, Solvent engineering for high-performance inorganic-organic hybrid perovskite solar cells, Nat. Mater. 13 (2014) 897.

[34] X. Li, D. Bi, C. Yi, J.-D. Decoppet, J. Luo, S.M. Zakeeruddin, A. Hagfeldt, M. Gratzel, A vacuum flash-assisted solution process for high-efficiency large-area perovskite solar cells, Science 353 (6294) (2016) 58.

[35] P.W. Voorhees, The theory of Ostwald ripening, J. Stat. Phys. 38 (1) (1985) 231–252.

[36] T.M. Koh, K. Fu, Y. Fang, S. Chen, T.C. Sum, N. Mathews, S.G. Mhaisalkar, P.P. Boix, T. Baikie, Formamidinium-Containing metal-halide: an alternative material for near-IR absorption perovskite solar cells, J. Phys. Chem. C 118 (30) (2014) 16458–16462.

[37] V.K. LaMer, R.H. Dinegar, Theory, production and mechanism of formation of monodispersed hydrosols, J. Am. Chem. Soc. 72 (11) (1950) 4847–4854.

[38] J. Chen, J. Song, F. Huang, H. Li, S. Liu, M. Wang, Y. Shen, The role of synthesis parameters on crystallization and grain size in hybrid halide perovskite solar cells, J. Phys. Chem. C 121 (32) (2017) 17053–17061.

[39] W. Zhu, L. Kang, T. Yu, B. Lv, Y. Wang, X. Chen, X. Wang, Y. Zhou, Z. Zou, Facile face-down annealing triggered remarkable texture development in CH$_3$NH$_3$PbI$_3$ films for high-performance perovskite solar cells, ACS Appl. Mater. Interfaces 9 (7) (2017) 6104–6113.

[40] Y. Wang, J. Li, Q. Li, W. Zhu, T. Yu, X. Chen, L.A. Yin, Y. Zhou, X. Wang, Z. Zou, PbI$_2$ heterogeneous-cap-induced crystallization for an efficient CH$_3$NH$_3$PbI$_3$ layer in perovskite solar cells, Chem. Commun. 53 (36) (2017) 5032–5035.

[41] W. Zhu, C. Bao, B. Lv, F. Li, Y. Yi, Y. Wang, J. Yang, X. Wang, T. Yu, Z. Zou, Dramatically promoted crystallization control of organolead triiodide perovskite film by a homogeneous cap for high efficiency planar-heterojunction solar cells, J. Mater. Chem. A 4 (32) (2016) 12535–12542.

[42] Y.K. Kim, B. Jeon, H.J. Park, Interfacial electronic structure of methylammonium lead iodide grown on a mesoporous TiO$_2$ layer on F-Doped tin oxide substrate, J. Phys. Chem. C 120 (39) (2016) 22460–22465.

[43] Q. Chen, H. Zhou, T.-B. Song, S. Luo, Z. Hong, H.-S. Duan, L. Dou, Y. Liu, Y. Yang, Controllable self-induced passivation of hybrid lead iodide perovskites toward high performance solar cells, Nano Lett. 14 (7) (2014) 4158–4163.

[44] H. Lee Yong, J. Luo, R. Humphry-Baker, P. Gao, M. Gratzel, K. Nazeeruddin Mohammad, Unraveling the reasons for efficiency loss in perovskite solar cells, Adv. Funct. Mater. 25 (25) (2015) 3925–3933.

[45] X. Wang, L.-L. Deng, L.-Y. Wang, S.-M. Dai, Z. Xing, X.-X. Zhan, X.-Z. Lu, S.-Y. Xie, R.-B. Huang, L.-S. Zheng, Cerium oxide standing out as an electron transport layer for efficient and stable perovskite solar cells processed at low temperature, J. Mater. Chem. A 5 (4) (2017) 1706–1712.

[46] J.-J. Li, J.-Y. Ma, J.-S. Hu, D. Wang, L.-J. Wan, Influence of N, N-dimethylformamide annealing on the local electrical properties of organometal halide perovskite solar cells: an atomic force microscopy investigation, ACS Appl. Mater. Interfaces 8 (39) (2016) 26002–26007.

[47] J.-J. Li, J.-Y. Ma, Q.-Q. Ge, J.-S. Hu, D. Wang, L.-J. Wan, Microscopic investigation of grain boundaries in organolead halide perovskite solar cells, ACS Appl. Mater. Interfaces 7 (51) (2015) 28518–28523.